

Correcting field-dependent aberrations with nanoscale accuracy in three-dimensional single-molecule localization microscopy

ALEX VON DIEZMANN,¹ MAURICE Y. LEE,^{1,2} MATTHEW D. LEW,^{1,3,4} AND W. E. MOERNER^{1,*}

¹Department of Chemistry, Stanford University, Stanford, California 94305, USA

²Biophysics Program, Stanford University, Stanford, California 94305, USA

³Department of Electrical Engineering, Stanford University, Stanford, California 94305, USA

⁴Current address: Department of Electrical and Systems Engineering, Washington University in St. Louis, St. Louis, Missouri 63130, USA

*Corresponding author: wmoerner@stanford.edu

Received 19 August 2015; revised 13 October 2015; accepted 19 October 2015 (Doc. ID 248290); published 19 November 2015

The localization of single fluorescent molecules enables the imaging of molecular structure and dynamics with sub-diffraction precision and can be extended to three dimensions using point spread function (PSF) engineering. However, the nanoscale accuracy of localization throughout a 3D single-molecule microscope's field of view has not yet been rigorously examined. By using regularly spaced subdiffraction apertures filled with fluorescent dyes, we reveal field-dependent aberrations as large as 50–100 nm and show that they can be corrected to less than 25 nm over an extended 3D focal volume. We demonstrate the applicability of this technique for two engineered PSFs, the double-helix PSF and the astigmatic PSF. We expect these results to be broadly applicable to 3D single-molecule tracking and superresolution methods demanding high accuracy. © 2015 Optical Society of America

OCIS codes: (180.2520) Fluorescence microscopy; (180.6900) Three-dimensional microscopy; (100.6640) Superresolution; (220.1010) Aberrations (global).

<http://dx.doi.org/10.1364/OPTICA.2.000985>

1. INTRODUCTION

The localization of single optical emitters to precisions of an order of magnitude or more below the diffraction limit is a powerful tool for biological wide-field microscopy. It is the foundation for single-particle tracking and (single-molecule) superresolution imaging, two techniques that have become increasingly popular in diverse areas of biophysics. In single-particle tracking, by localizing a single fluorescent or scattering particle over multiple frames, a spatial trajectory of that particle can be generated, allowing the measurement of particle diffusion and interactions [1–5]. Alternatively, by actively switching an ensemble of fluorescent emitters between dark and bright states such that only a few spatially resolved bright emitters appear in any one wide-field camera frame, the entire ensemble can be localized to subdiffraction precision in a time-sequential fashion, allowing the reconstruction of a “superresolved” image of the emitters’ underlying spatial distribution [6–10]. Techniques based on particle localization have been implemented with single fluorescent molecules and with scattering or luminescent nanoparticles; we refer to these generally as “molecules” below.

Recently, several microscope modifications have extended single-molecule localization to three dimensions, which is necessary for a full understanding of complicated biological systems. Without these modifications, it is difficult to extract 3D position

information because the standard microscope point spread function (PSF) changes slowly in the axial (z) dimension and does so symmetrically above and below the focal plane. Modifications of the detection optics that overcome this limitation include sampling the PSF of the molecule at different focal positions [11], using self-interference [12,13], or engineering the shape of the PSF to encode additional information [14–17]. With each method, it is possible to greatly improve the precision of axial (z) localization without severely compromising transverse (xy) localization.

In both 2D and 3D single-molecule localization, scientists fit the observed image of the molecule’s PSF using an appropriate estimator [18,19]. The resolving power of tracking and imaging experiments depends on both the precision and accuracy of this estimation [20]. In general, the statistical precision of emitter localization, as defined by the standard deviation of repeated localizations, is limited by the molecule’s photophysics, scaling in leading order with the inverse of the square root of the number of photons collected [21,22]. Measurements using fluorescent proteins, which emit $\sim 10\times$ fewer photons before photobleaching than small organic molecules, typically allow localization precisions of the order of 15–40 nm [12,23], while the brightest organic dyes can be localized down to 1–10 nm precision [24–26]. To match this high precision, modern localization techniques

require extremely accurate and well-calibrated systems, as any systematic error ≥ 10 nm distorts such fine measurements, leading to misestimation of the sizes of superresolved structures or of displacements during tracking. A 3D imaging system faces even more stringent requirements, as it must perform accurately even when an emitter is defocused by hundreds of nanometers. For example, defocus can cause >100 nm mislocalization errors due to the dipole orientation of rotationally constrained molecules [27–30], and molecules deep in the sample can suffer from z localization errors due to the aberrations and focal shift produced by refractive index mismatch [31–33], the latter of which should always be corrected in advance. One source of error that has not, to our knowledge, been explored in detail is the effect of field-dependent aberrations on localization accuracy. Previous studies have demonstrated the necessity of sampling the microscope PSF throughout the full observable 3D volume of the microscope when registering multiple channels [23,34], implying field-dependent variation in 3D PSFs throughout the transverse field of view (FOV). However, there does not currently exist a robust, systematic method for defining this PSF variation, and the variation is not accounted for in current estimators.

Here, we report a novel approach to simultaneously measure and correct the field-dependent PSF variations of a 3D localization microscope. To do this, we fabricated subdiffraction-sized nanohole arrays (NHAs) in a metal film on a standard glass cover-slip, similar to standards used previously for 2D imaging [35–38]. By filling a NHA with fluorescent dyes in aqueous solution on the free surface, we generate a regularly spaced array of point emitters at a selected wavelength. We use the NHA as a calibration standard for 3D localization microscopy to finely sample the 3D PSF of the microscope throughout the FOV, demonstrating the impact of field-dependent effects on two 3D PSF designs: the double helix PSF (DH-PSF) [16] and the astigmatic PSF [14,15]. In both cases, we find errors in z localization as a function of field position on the order of 20% (e.g., 40 nm error for a 200 nm displacement) throughout even the relatively small (tens of micrometers) FOV of standard 3D localization microscopes. We demonstrate that these errors can be corrected by using local calibration functions generated using the NHAs.

2. THEORY AND METHODS

A. Effect of Field-Dependent Aberrations on Fourier Processing in a 3D Localization Microscope

Optical Fourier processing is a method used in many different areas of imaging to encode additional information by modulating the spatial Fourier transform of the image [39]. This can easily be done using the Fourier transform properties of lenses: a lens appropriately positioned relative to a spatially coherent light source will generate a scaled Fourier transform of the image of that source. In localization microscopy, single molecules act as self-coherent sources, while the back focal plane of the objective contains the Fourier transform of the image. By modulating the spatial frequency components of the emission, it is possible to encode properties of the emitter, such as dipole orientation, rotational mobility, emission spectrum, and depth (z position), into the microscope's PSF [40,41].

For convenience, a Fourier plane (FP) conjugate to the back focal plane is often created downstream of the intermediate image plane by using a $4f$ system consisting of two lenses, with a phase

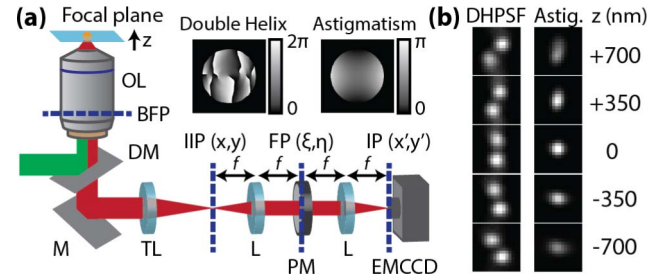


Fig. 1. (a) Schematic of a $4f$ optical processing system using a transmissive phase mask. The full illumination path is not shown but is typical of a wide-field epifluorescence microscope, with illumination (green) provided by lasers coupled up to the sample, and collected fluorescence (red) sent through a separate detection path. BFP, back focal plane; PM, phase mask; FP, Fourier plane; IIP, intermediate image plane; IP, image plane; L, lens; OL, objective lens; TL, tube lens; DM, dichroic mirror; M, mirror; EMCCD, electron-multiplying charge-coupled device camera. Inset: the DH-PSF and astigmatism phase mask patterns. (b) Images of the DH-PSF and astigmatic PSF at various levels of defocus, as taken from a calibration scan acquired with fluorescence from a single hole of a NHA (Fig. 2), using a SLM to generate the double-helix and astigmatism phase patterns. (Pixel size = 160 nm.)

mask placed between them to modulate the FP (Fig. 1). (While the mask could alter both amplitude and phase, the reduction in signal, and thus localization precision, from absorptive masks renders phase-only masks greatly preferable.) Formally, this process can be written as

$$E_2(x',y') = \mathcal{F}\{e^{i\psi(\xi,\eta)}\mathcal{F}\{E_1(x,y)\}\}, \quad (1)$$

with \mathcal{F} the Fourier transform operator, $E_1(x,y)$ and $E_2(x',y')$ the electric fields in the intermediate and final image planes, respectively, and $\psi(\xi,\eta)$ the phase function of the phase mask in the FP [Fig. 1(a)]. This approach is common to many PSFs engineered by Fourier processing, with the choice of phase mask being the fundamental difference between them.

While the formalism of Fourier optics provides an instructive guide to optical processing, it is strictly an ideal imaging model. Specifically, the approach detailed above inherently assumes that the imaging system is isoplanatic, or space-invariant, which is not strictly true for real systems. In the syntax of linear systems, the imaging system of a 3D localization microscope described in Eq. (1) could be equivalently written as the convolution integral

$$E_2(x',y') = \iint_{-\infty}^{\infty} g(x'-x, y'-y) E_1(-x, -y) dx dy, \quad (2)$$

where the phase mask generates a shift-invariant impulse response applied to the input electric field $E_1(x,y)$, i.e., $g = \mathcal{F}\{e^{i\psi(\xi,\eta)}\}$. We can use the formalism of phase delays in the Fourier/pupil plane to approximately describe the effect of possible distortions of the optical system. As a simple case, we can describe the image of a molecule placed away from the focal plane (i.e., $z \neq 0$), by adding a quadratic phase term $a(\xi^2 + \eta^2)$, $a \propto z$, such that $g = \mathcal{F}\{e^{i\psi(\xi,\eta)} e^{ia(\xi^2 + \eta^2)}\}$. (This phase delay is physically introduced before the intermediate image plane at (x,y) is formed, but it is mathematically equivalent to consider it as a phase added to the ideal input E_1 formed by a molecule at the focal plane. Note that a full treatment of defocus for high-NA optics properly includes higher order terms.) While defocus changes the appearance of the image, the imaging system is still shift-invariant. This

property can also be true in the presence of some aberrations. These aberrations can be described using various schemes, including the Zernike polynomials. For the purposes of this illustration, it is expedient to speak in terms of the Seidel aberrations, as they explicitly recognize field dependence. Therefore, spherical aberration introduces a phase delay $b(\xi^2 + \eta^2)^2$ for a constant b proportional to the strength of the aberration [42,43], giving $g = \mathcal{F}\{e^{i\psi(\xi,\eta)} e^{ib(\xi^2+\eta^2)^2}\}$. While this aberration distorts the PSF from its ideal form, it is distorted identically everywhere across the FOV, meaning that the PSF is defined by the response of a single point source (indeed, it is even possible to compensate for this aberration in the imaging system with the mask $\psi(\xi,\eta)$ [44–46]). However, we cannot expect this shift-invariant property to hold for all aberrations of the imaging system. While it is common to consider aberrations as shift-invariant wavefront delays in the pupil, the strength of many aberrations varies as a function of position in the field that must be taken into account for large FOVs or for demanding measurements [42,43,47]. For example, the phase delay in the presence of field curvature scales as $(\xi^2 + \eta^2)(x^2 + y^2)$; that is, the degree of defocus is effectively a function of position in the FOV. Thus, the impulse response in the Fourier plane in the presence of field curvature is $\mathcal{F}\{e^{i\psi(\xi,\eta)} e^{c(\xi^2+\eta^2)(x^2+y^2)}\}$. This mixing of Fourier and image space coordinates reduces the convolution of Eq. (2) to a superposition integral:

$$E_2(x',y') = \iint_{-\infty}^{\infty} h(x',y';x,y) E_1(-x,-y) dx dy, \quad (3)$$

where the impulse response of the $4f$ system is explicitly dependent on the position (x,y) of the molecule. That is, the appearance of the PSF will vary depending on the field coordinates (x,y) . Further, if these fine variations are not accounted for properly, they will cause errors in measurements derived from the PSF, such as 3D position. In general, single-molecule microscopes use the best-corrected objectives and optics available, but even the best optics do not guarantee the absence of aberrations on the order of tens of nanometers when imaging over a FOV of tens of micrometers, especially considering the high-NA objectives required for single-molecule imaging. Importantly, these errors cannot be easily removed by phase retrieval or manipulation in the Fourier plane. To our knowledge, the shift-invariance of 3D PSFs used for single-molecule localization has not been explicitly tested, and given the demanding accuracy requirements of single-molecule localization microscopy, it behooves us to measure whether the aberrations of the imaging system create errors on the scale of tens of nanometers, and if so, to provide a means for their correction.

B. Optical Instrumentation

The 3D measurements in this study were performed using two home-built wide-field fluorescence microscopes. The first is described in [23], using a geometry similar to that illustrated in [Fig. 1(a)]. Briefly, illumination was provided by a 100 mW 561 nm laser (sapphire 561 LP, Coherent) in an epi-illumination geometry. The fluorescence from the sample was collected by a high-NA super-corrected oil-immersion objective (Olympus PLAPON60XOSC, 60X/NA1.4) and filtered by an appropriate dichroic and bandpass filter. The intermediate image plane was formed by an $f = 400$ mm tube lens, followed by a $4f$ system composed of lenses with $f = 120$ mm, matching the 2.7 mm

diameter of the transmissive quartz phase mask encoding the DH-PSF (Double-Helix Optics, LLC). The modulated image was detected on a Si EMCCD camera (Andor iXon DU-897E).

The second setup uses the two-channel pyramid geometry described in [48] with a programmable phase modulator. Samples were illuminated with a 100 mW 641 nm laser (CUBE 640-100C, Coherent). Fluorescence was collected by a high-NA oil-immersion objective (Olympus UPLSAPO100XO, 100X/NA1.4) and filtered by the appropriate dichroic beam splitter and bandpass filter. Fluorescence was passed through a polarizing beam splitter (B. Halle PTW 20) before being directed through a $4f$ system incorporating a liquid crystal phase-only spatial light modulator (Boulder Nonlinear Systems XY Phase Series) encoding the phase mask. For simplicity, the results from only one of the polarization channels of the setup are described, but both channels showed similar behavior, and polarization is not the central focus of this study.

C. Fabrication of Nanohole Arrays

The NHAs were fabricated as follows. First, high-tolerance coverslips (Schott Nexterion #1.5H) were cleaned using the SC1/SC2 sequence of a standard RCA clean (i.e., $\text{NH}_3/\text{H}_2\text{O}_2$ and $\text{HCl}/\text{H}_2\text{O}_2$) prior to deposition of ~ 100 nm Al via electron-beam (e-beam) evaporation (Innotec ES26C). Nanohole patterns were generated using single-shot dot exposures onto spin-coated e-beam resist (ZEP520A, ZEON Corp.) using a RAITH150 e-beam writer. The resist was developed in xylenes followed by a mixture of methylisobutylketone/isopropanol (1:3 MIBK/IPA) and a final IPA rinse. The hole pattern was transferred to the aluminum by dry etching with a Versaline LL-ICP metal etcher with Cl_2/BCl_3 plasma, and resist was removed with an *N*-methyl-2-pyrrolidone-based stripper (Remover PG, Microchem) followed by an IPA rinse. SEM images of the holes were acquired using the RAITH150 in SEM mode.

D. Microscopy with Fluorescent Beads and NHAs

Fluorescent beads (100 nm 540/560 or 100 nm 625/645 FluoSpheres, Life Technologies) were immobilized in a 1% polyvinyl alcohol (PVA) film on a #1.5 coverslip and covered with a drop of water during the measurement in order to mimic the refractive index mismatch of typical single-molecule cellular imaging experiments. NHAs were filled with dyes by depositing ~ 10 – 50 μl of aqueous solution containing ~ 50 μM of the chosen dye (Alexa 568 or Alexa 647, Life Technologies) on top of the aluminum surface of the NHA. The NHAs were cleaned for reuse either by several washes with water or with a solvent rinse series (hexanes, isopropanol, ethanol, and water). We separately confirmed that the emission from the NHA holes was not polarized by comparing images from the reflected and transmitted channels of the polarizing beam splitter, measuring an emission polarization $P = (I_R - I_T)/(I_R + I_T)$ of 0.018 ± 0.025 (mean \pm s.d., $N = 369$ nanoholes).

Calibration measurements with NHAs and localization experiments with the fluorescent beads acting as single test emitters were performed similarly. Images of either set of emitters were acquired at each of a series of microscope objective defocus steps generated using a nanopositioner (C-Focus, Mad City Labs). The objective was translated axially (in z) in 50 nm steps from -1 μm to $+1$ μm relative to focus, with enough frames to allow for relaxation of the objective and sample. In the following

experiments, we collected 5000–200,000 photons per bead or nanohole per 50 ms frame. This photon flux corresponds to an empirical localization precision in each frame of 1–5 nm in xy and 2–10 nm in z for the DH-PSF, as calculated from the standard deviation of successive localizations, scaling roughly with the inverse root number of photons detected. By averaging over 5–8 frames, we detected a total of 10^4 – 10^6 photons from each emitter at each step, with a typical precision for the averaged positions of 0.5–1 nm in xy and 1–2 nm in z . The reproducibility of the objective's positioning was checked in each calibration by comparing scans moving up and then immediately back down through the 2 μm travel distance, and there was a <25 nm difference in the observed z position of the sample at any step between the scans.

E. Image Processing and Analysis

Analysis was performed using scripts written in MATLAB (The Mathworks, Inc., Natick, Massachusetts). Calibration and fitting analysis of DH-PSF images were performed using a modified version of open-source Easy-DHPSF software (<https://sourceforge.net/projects/easy-dhpsf/>, [49]). When analyzing images of the DH-PSF, the lobes of each PSF were fit using the *lsqnonlin* least-squares function of MATLAB with a pair of identical, radially symmetric Gaussians as the objective function. Images of the astigmatic PSF were fit using an elliptical Gaussian, with z extracted by finding the best match to model functions of the widths $w_x(z)$, $w_y(z)$ extracted from a selected calibration nanohole [15]. Images of the beads were fit using the NHA calibrations, with z positions extracted either from the calibration of a “central nanohole” or using the nanohole closest in xy to each bead. Interpolated surfaces between data points from sets of nanoholes or beads used for visualization purposes were generated with the *scatteredInterpolant* built-in MATLAB function using “natural” interpolation. It is worth noting that neither the DH-PSF nor the astigmatic PSF is exactly a Gaussian shape and that a maximum likelihood estimation (MLE) approach based on actual PSF shapes might be superior, but these estimators are in common use, and it is the purpose of the calibration procedure to define the relationship between fit parameters and actual 3D positions.

3. RESULTS AND DISCUSSION

A. Motivation and Approach for Measuring Field-Dependent Effects

Previous experiments in multichannel 3D registration [23] have shown that it is necessary to finely sample the 3D FOV to achieve single-molecule registration accuracy of <10 nm, implying fine field-dependent differences between the imaging systems of each channel. *A priori*, this observation implies that behavior of one or both channels varies with field position, which could represent an unknown systematic error for 3D localization. In typical practice, the 3D response of a PSF (e.g., the rotation of the line connecting the two lobes as a function of defocus, $\theta(z)$, for the DH-PSF, or the library of images utilized in MLE) is calibrated by extracting x , y , z from imaging the apparent PSF for a single emitter while scanning the objective up and down in z (Fig. 1). This single, global calibration does not sample field-dependent variations. While in principle it would be possible to scan one or several fluorescent beads throughout the 3D volume, as has been

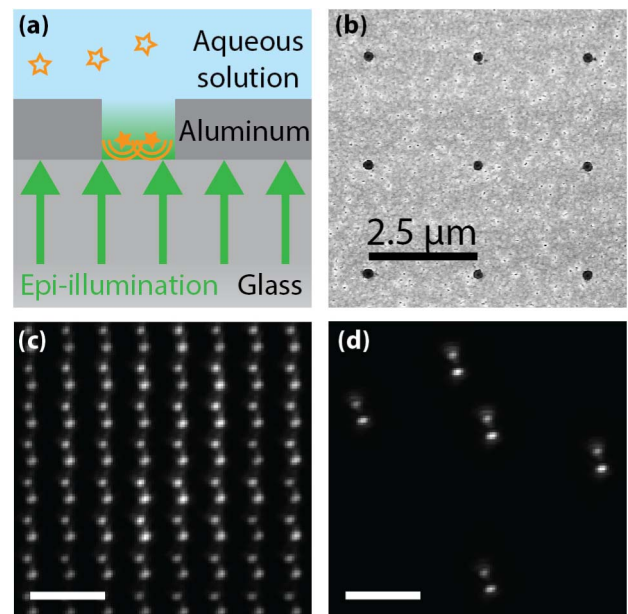


Fig. 2. Subdiffraction holes in a NHA function as regularly spaced fluorescent point emitters. (a) Schematic depicting nanohole geometry. Wide-field epi-illumination (green) passes through the glass coverslip into a nanohole etched into a layer of aluminum. An aqueous solution of fluorescent dyes fills the nanohole from the top, and the spatially restricted light emitted from dyes diffusing within the nanohole (orange) is detected from below, as shown in Fig. 1, mimicking a point emitter. (b) Scanning electron microscope image of a NHA, showing the pitch of 2.5 μm and hole diameters of ≤ 200 nm. (c) Images of the DH-PSF acquired using the NHA in (b) when filled with fluorescent dyes. Scale bar: 5 μm . (d) Images of the DH-PSF as generated by 100 nm diameter fluorescent beads acquired using the same optical configuration as in (c).

done for 2D registration [50–52], the additional delay from scanning in z (10–50 s for each scan) makes bead scanning more difficult, as nanoscale drift of the microscope stage between scans and bleaching of the beads can introduce systematic differences between calibrations that do not reflect true field-dependent variation of the optical instrument.

To simultaneously sample the entire FOV with bright point emitters, we fabricated NHAs for use as 3D calibration standards [Figs. 2(a) and 2(b)] (see Section 2.C for details). The NHAs consist of subdiffraction (≤ 200 nm) apertures with a regular spacing of 2.5 μm , etched in aluminum film on high-tolerance #1.5 glass coverslips. To generate emission patterns approximating those from a point emitter, we filled the nanoholes with an aqueous solution of fluorescent dyes and excited the dyes with wide-field illumination. The resulting emission patterns closely resembled those of 100 nm fluorescent beads [Figs. 2(c) and 2(d)]. Due to the large reservoir of fluorescent dye, these samples are effectively unbleachable, enabling calibrations with constant and very bright emitter intensity throughout the entire 3D FOV.

B. Measurement of Field-Dependent Effects on 3D Localization

We began by measuring the variation in 3D response of an imaging system using a transmissive phase mask to generate the double-helix PSF [23]. The 3D response measured with the NHA had a large degree of field-dependent variation, as can

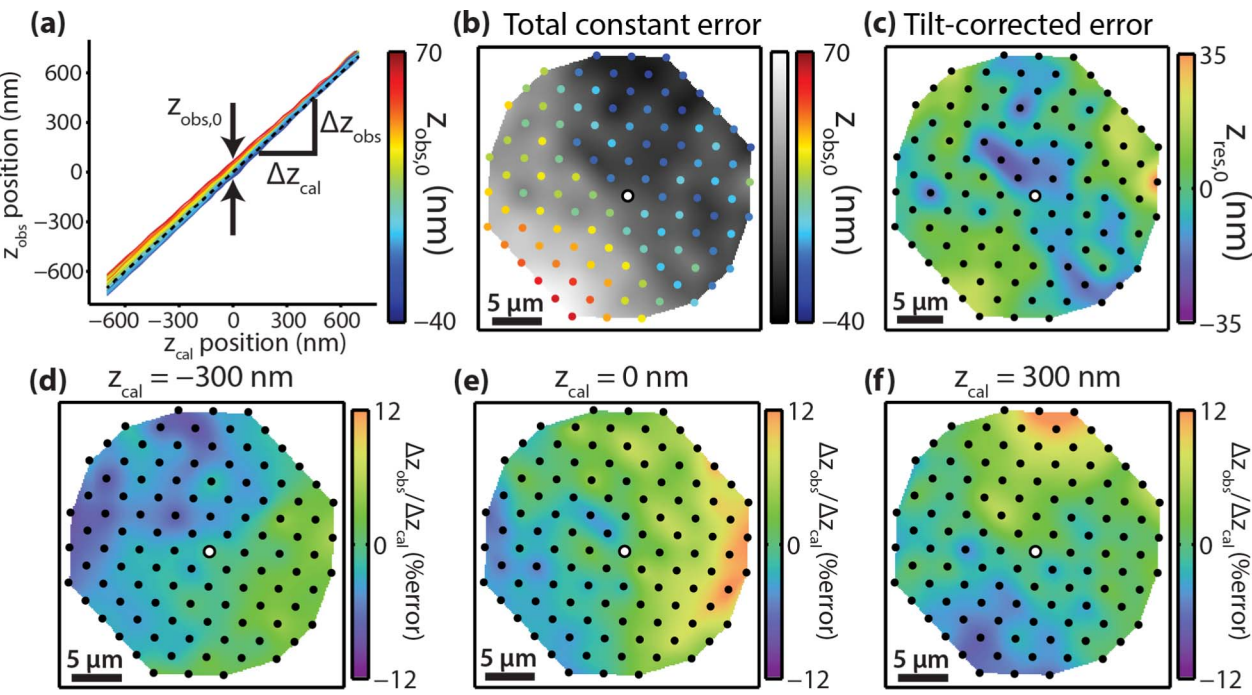


Fig. 3. Calibration scans using a NHA reveal field-dependent variations in the response of the DH-PSF for a setup using a transmissive phase mask. (a) The observed z positions, z_{obs} , from a simultaneous z -scan of >100 nanoholes within a $\sim 30 \mu\text{m}$ FOV. The z positions are extracted from the DH-PSF images of each nanohole using the calibration function $\theta(z)$ generated from a single nanohole over the defocus range z_{cal} . The variation in z_{obs} (colored lines) relative to the calibration nanohole (dotted black line) is described by a constant error $z_{\text{obs},0}$ ranging from -40 to 70 nm in addition to a variation in PSF response accuracy $\Delta z_{\text{obs}}/\Delta z_{\text{cal}}$, which itself changes over the calibration z range. (b) The interpolated spatial variation of $z_{\text{obs},0}$ (gray scale) between nanoholes [dots colored as in (a), calibration nanohole marked in white]. (c) The spatial variation of the residual errors in $z_{\text{obs},0}$ after removing planar sample tilt, $z_{\text{res},0}$. (d-f) The variation in DH-PSF 3D response described as the fractional departure of $\Delta z_{\text{obs}}/\Delta z_{\text{cal}}$ from unity, i.e., $(\Delta z_{\text{obs}} - \Delta z_{\text{cal}})/\Delta z_{\text{cal}}$, at (d) -300 nm , (e) 0 nm , and (f) $+300 \text{ nm}$ defocus, interpolated between nanoholes. Note that the total magnitude of variation ($\sim 60 \text{ nm}$) is substantially greater than the effective z localization precision of the holes at each z_{cal} step ($\sim 2 \text{ nm}$).

be visualized by comparing the calibrations measured from nanoholes across the FOV (Fig. 3). Each calibration of the DH-PSF generates a curve $\theta(z_{\text{cal}})$ for lobe angle θ at known z_{cal} positions defined by the precision axial translator. (In practice, the extracted xy positions from the midpoint between the two lobes at each z should all be the same since only z translation is done; however, there is apparent xy motion with z that is always removed from the final position determinations. This part of the calibration is described in Fig. S1 in *Supplement 1* since the focus here is on axial position.) To measure the variation across the FOV, we first used the calibration curve from a central nanohole [dotted line in Fig. 3(a), white dot in Figs. 3(b)–3(f)] as a global calibration to fit the observed $\theta(z_{\text{cal}})$ values of each other hole, giving an observed z value z_{obs} at each z position. Thus, $z_{\text{obs}} = z_{\text{cal}}$ for the calibration nanohole by definition, and values of z_{obs} that differ from the z_{cal} , indicate field-dependent z estimation errors at other nanohole positions, as is clearly visible in the range of calibrations in [Fig. 3(a)].

These errors can be described by two components: an offset $z_{\text{obs},0}$, the difference in z_{obs} when in focus at $z_{\text{cal}} = 0$, and a multiplicative error in the z response of the PSF, $\Delta z_{\text{obs}}/\Delta z_{\text{cal}}$, that describes how the calibration curves have differing nonunity slopes over the range z_{cal} . [Fig. 3(a)]. To present the field dependence of the errors without assuming a specific aberration model, we interpolated between nanoholes. We found that the values of $z_{\text{obs},0}$ had a clear field dependence, manifesting as a fairly smooth surface ranging from -40 to 70 nm over the FOV [Fig. 3(b)]. A large

component of this field variation persisted after correcting for planar sample tilt: the residual error $z_{\text{res},0}$ ranged over $\sim 60 \text{ nm}$ [visualized as a curved surface in Fig. 3(c)]. This variation of $z_{\text{obs},0}$ represents a nanoscale aplanarity of the image created by the system, as would be expected for high-magnification objectives. To confirm that this was an effect of the optics, rather than of variation in the sample (i.e., roughness or different nanohole etch profiles), we translated and rotated the sample, and found that these results did not change with the position or orientation of the NHA (Fig. S2 in *Supplement 1*). (In practice, such a test should be performed for every sample used to calibrate field dependence.). If left uncorrected, this optical variation creates an xy -dependent offset in z values measured for the object, such that a plane of emitters would exhibit an artifactual curvature when localized.

The second type of error, $\Delta z_{\text{obs}}/\Delta z_{\text{cal}}$, was calculated as the tangent of the curves $z_{\text{obs}}(z_{\text{cal}})$, i.e., the fractional departure from unity slope for a finite displacement, $(\Delta z_{\text{obs}} - \Delta z_{\text{cal}})/\Delta z_{\text{cal}}$ [Fig. 3(a)], evaluated at multiple values of z_{cal} . We found that the slopes had a total variation of $\sim 20\%$ over the FOV, with the “shape” of the field dependence changing dramatically as a function of z position [Figs. 3(d)–3(f), and Figs. S2 and S3 in *Supplement 1*]. Intriguingly, these shapes resemble a tilted plane that rotates with changing z_{cal} , similar to the rotation of the DH-PSF. However, while we consistently observe a similar “tilted plane”-like feature in the response error in other experiments using the DH-PSF (e.g., Fig. 4), the feature does not always rotate, suggesting that this behavior does not arise from the DH-PSF itself.

Thus, rather than a simple 2D scan, a full 3D calibration scan is needed to remove these errors. This field-dependent error stretches the measured z heights of localized emitters: for example, at (x, y, z) positions for which the response error is $+10\%$, two emitters separated by a true z distance of 100 nm would appear to be separated by 110 nm if using the global calibration. A range of 20% error would lead to distance estimates ranging from 90 to 110 nm across the FOV. Generating the global calibration from a different nanohole or an average of nanoholes would still give field-dependent errors and simply shifts the parts of the FOV containing errors.

To compare the effects of these field-dependent aberrations on different PSFs, we also measured the field-dependent errors present when using a spatial light modulator to encode either the DH-PSF or an astigmatic PSF [48]. (For these experiments, we used a lower-strength astigmatism mask than is typically used for single-molecule experiments. This modification lets us extend the z range of the astigmatic PSF, which typically has a range of $\sim 1\text{--}1.2 \mu\text{m}$, to be closer to that of the DH-PSF, which has a working range of $\sim 2 \mu\text{m}$.) We observed that the PSFs generated from both phase masks had an similar field dependence for $z_{\text{obs},0}$, as would be expected for 3D imaging using a microscope with position-dependent phase delays [Figs. 4(a) and 4(d)]. The magnitude and direction of the planar tilt were identical for the two PSFs, as would be expected for a tilt in the mapping of the sample plane to the image plane that resulted from sample tilt or a slight misalignment of the optics. However, the magnitude of the non-planar component of the errors was significantly higher for the astigmatism mask [Figs. 4(b) and 4(e)]. Additionally,

the response errors $\Delta z_{\text{obs}}/\Delta z_{\text{cal}}$ were markedly different between phase masks. While the range of errors was approximately 20%–30% over the FOV for both cases, the distribution of errors across the field was different. [Figs. 4(c) and 4(f), and Figs. S4 and S5 in Supplement 1].

Since both phase masks were encoded by the same spatial light modulator, this dissimilarity is not a result of different alignment of the masks. Rather, we conclude that the field-dependent aberrations affect different 3D PSFs differently depending on the design of the phase mask. This effect can be understood in terms of the specific features of the PSF that encode the z position of the emitter: for example, we can expect that an astigmatic PSF would be more sensitive than the DH-PSF to field-dependent astigmatic aberrations. Another consideration is the relative strength of the PSF's phase mask $\psi(\xi, \eta)$ versus the strength of the phase function $\phi(\xi, \eta; x, y)$ that characterizes the aberrations of the optical system. Since the astigmatism phase mask imparts less of a phase delay in the FP than the DH-PSF [Fig. 1(a)], the astigmatic PSF is perturbed more than the DH-PSF by an identical aberration phase function $\phi(\xi, \eta; x, y)$ acting on both PSFs. Further, the singularities of the DH-PSF phase mask are robust features in the Fourier plane, which reduces the DH-PSF's sensitivity to relatively low-frequency (i.e., smooth) aberrations. In a separate experiment, we also observed that changing the objective lens, even to another objective of the same specifications from the same manufacturer, subtly changed the form of the “response error” of both PSFs (Figs. S6 and S7 in Supplement 1), underscoring the sensitivity of the 3D imaging system to changes in the optical components and the need for careful calibration.

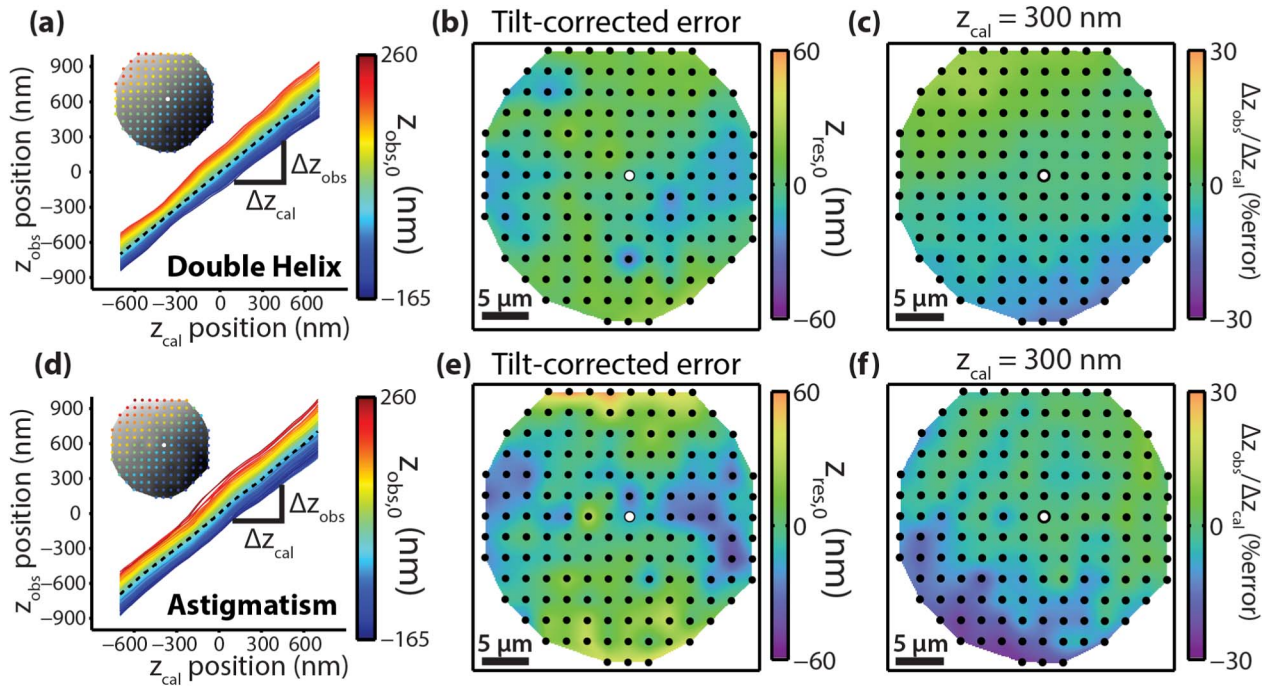


Fig. 4. Calibration scans using a NHA compare the field-dependent variations in the response of the DH-PSF and the astigmatic PSF, with the phase masks encoded using a spatial light modulator. (a)–(c) describe the DH-PSF and (d)–(f) describe the astigmatic PSF. (a), (d) The observed z positions, z_{obs} (colored lines), from a simultaneous z -scan of >150 nanoholes within an $\sim 33 \mu\text{m}$ FOV. The images generated from each nanohole were fit using the calibration function generated from a single nanohole over the range of defocus positions z_{cal} , with the black dotted line describing the response of the calibration nanohole. Inset: the interpolated spatial variation of $z_{\text{obs},0}$ with nanohole positions marked as color-coded dots. (b), (e) The spatial variation of the residual errors in $z_{\text{obs},0}$ after removing planar sample tilt, $z_{\text{res},0}$. (c), (f) The variation in 3D response described as the fractional departure of $\Delta z_{\text{obs}}/\Delta z_{\text{cal}}$ from unity, i.e., $(\Delta z_{\text{obs}} - \Delta z_{\text{cal}})/\Delta z_{\text{cal}}$, at $+300$ nm defocus. White dots: calibration nanohole.

C. Correction of Field-Dependent Mislocalization Error

The field-dependent variations we observe lead to a range of systematic z localization errors on the order of 20%. For z distances common to some single-molecule imaging experiments (~ 50 – 200 nm), this percentage represents a systematic error of ~ 10 – 40 nm, on the order of typical localization precision, and more for larger axial ranges. For localization data to be meaningful, it is necessary to reduce the systematic error significantly below the photon-limited precision. A straightforward way to correct these field-dependent errors is to use a locally varying calibration function generated by interpolating the many calibrations from the NHA. To demonstrate this approach, we scanned fluorescent beads attached to the coverslip throughout z , estimating bead positions either with the global calibration $z(\theta)$ from one central nanohole (position as shown in Fig. 3) irrespective of the bead's position in the FOV, or with a local calibration $z(\theta; x, y)$ obtained from the nanohole nearest to each bead.

To quantitate the “stretching” effect of field-dependent errors, we measured the errors in the observed z displacements, $\Delta z_{\text{obs}} - \Delta z_{\text{cal}}$, which describe the z mislocalization of each bead relative to the set of displacements z_{cal} . These errors were greatly affected by our calibration strategy. When using a global calibration (as shown in Fig. 3), each bead exhibited localization errors scaling with total displacement [Fig. 5(a)]. The magnitude ($\sim \pm 8\%$) and field dependence of these errors matched those observed in the calibrations using the NHA [Figs. 5(a), 5(b), and 3(d), and Fig. S3 in Supplement 1], indicating that this systematic localization error was well described by the PSF variation observed with the NHA. We found that switching to a local cal-

ibration removed most of the apparent field-dependent errors: while there was still a random error in bead localizations, the systematic errors when using the global calibration were reduced from a maximum error of ~ 50 – 100 nm at the edge of the FOV to ≤ 25 nm for the full z range [Figs. 5(c) and 5(d)]. We note that the beads themselves appeared randomly offset from the surface of the coverslip (Fig. S8 in Supplement 1); this variation may represent roughness in the PVA film or heterogeneity of the distributions of fluorophores on each bead, and contributes to the errors we observe in this measurement of 3D PSF response.

To measure the *typical* magnitude of these field-dependent errors, we calculated the root-mean-square error interpolated between the beads at each z position [such as the surfaces shown for a displacement of -300 nm in Figs. 5(b) and 5(d)]. These errors remained at or below 7 nm over a >1.2 μm z range when using the local calibration, while this error was far larger even for small (~ 150 nm) axial displacements when using the global calibration, increasing roughly linearly to over 15 nm for large displacements [Fig. 5(e)]. This error includes both the localization error of the beads and bead-to-bead variability. To describe the *maximum* systematic errors over our FOV, we employed an additional metric, fitting the errors as a function of position to a plane and extrapolating the resulting gradient to a 30 μm FOV. Using this metric, we found that the systematic z -dependent error was removed for the local calibration, with only minor (<20 nm) residual random fitting errors. By contrast, the global calibration resulted in systematic errors that increased rapidly with z displacement, to 40 nm after 150 nm displacement, and continuing to increase to 80 nm after 600 nm displacement [Fig. 5(f)].

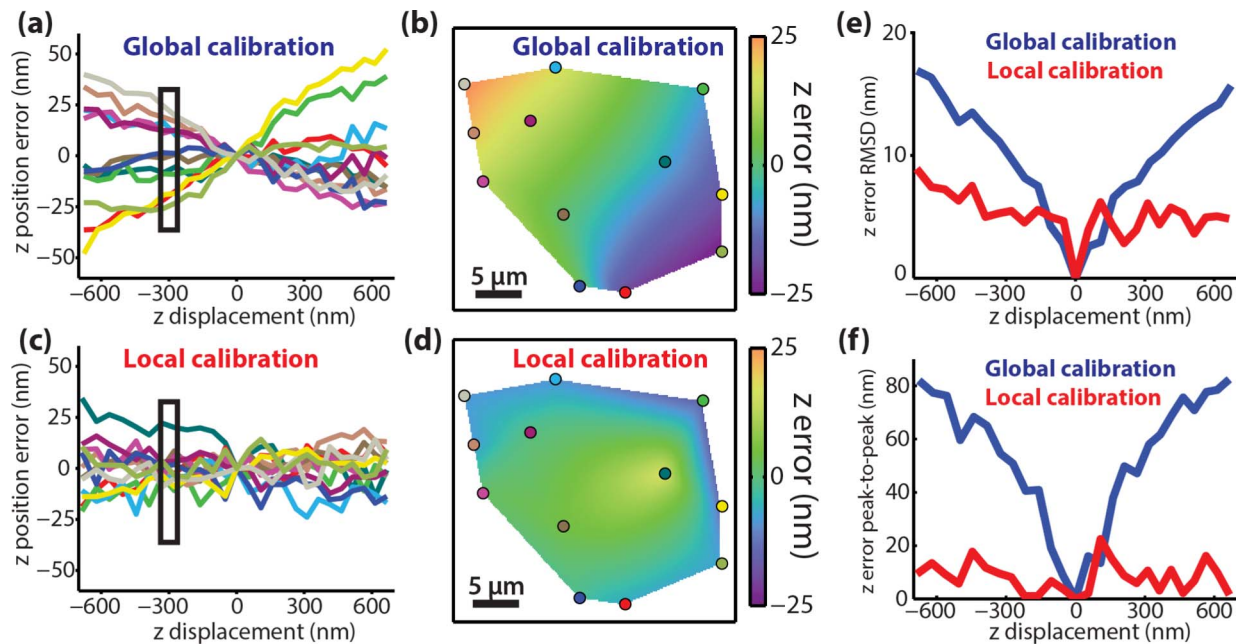


Fig. 5. Field-dependent z localization error for the DH-PSF imaging system characterized with a NHA in Fig. 3 is measured using fluorescent beads as test emitters and is reduced by using local rather than global calibrations. (a) The errors in 3D single-emitter localization when using a global calibration (nanohole shown in Fig. 3) for z position estimation throughout the FOV, measured as a function of z displacement relative to an initial position ($z = 0$). (b) The field dependence of localization errors in (a) at $z = -300$ nm, with dots marking the positions of each bead, colored as in (a). (c) The errors for the single-emitter data in (a) when using a local calibration. (d) The field dependence of localization errors in (c) at $z = -300$ nm, with dots marking the positions of each bead, colored as in (d). (e) The z -localization errors for the FOV over the z range of -700 to 700 nm, described as the standard deviation of the surface interpolated between beads at each z slice. (f) The peak-to-peak range of the systematic errors for a 30 μm FOV over the z range of -700 to 700 nm, calculated from a plane fit to the errors at each z slice.

4. CONCLUSIONS

In this work, we demonstrate a novel approach to measure the accuracy, rather than the precision, of 3D single-emitter localization over a microscope's field of view. We found that filling an array of subdiffraction nanoholes with a fluorescent dye solution generates precisely spaced point emitters that are useful for accurate 3D calibration measurements. By finely sampling two 3D PSFs throughout the FOV, we observed that our single-molecule microscopes exhibit a z -dependent localization error that leads to a "stretching" of 3D measurements of the order of $\sim 20\%$. The fine spacing of the nanoholes allowed us to correct these errors locally, keeping the typical error over a $>1.2 \mu\text{m}$ z range at or below 7 nm, including random localization error.

As localization precision improves with newly designed fluorescent labels and other methodological improvements, the need to also guarantee localization accuracy over the FOV becomes increasingly urgent. Single-molecule experiments that reach sub-nanometer precision in two dimensions require careful estimation of detector nonuniformity and dipole mislocalization errors [25,53], and we expect that the extension of these ultraprecise experiments to three dimensions will also require that field-dependent aberrations be carefully corrected. Another relevant trend is the increased use of sCMOS rather than EMCCD detectors for single-molecule localization [54]. The newer detectors generally afford larger FOVs, over which field-dependent errors will be exacerbated, thereby limiting these new instruments' utility for accurate 3D imaging unless these errors are corrected.

Here, we provide a robust methodology to measure and correct field-dependent aberrations in single-molecule microscopy that complements current techniques for correcting pupil aberrations. The approach we have demonstrated can be generally applied to 3D single-particle tracking or superresolution imaging experiments requiring nanoscale accuracy. While we have focused on measurements using PSFs generated by Fourier plane engineering, we expect that these field-dependent aberrations also negatively impact measurements using interferometry or multiplane imaging. We expect that the introduction of NHAs for use as 3D calibration samples will provide a convenient measurement tool to test the design of new systems and optics used for 3D localization, and correct any errors that remain after all else is optimized.

Funding. National Institute of General Medical Sciences (NIGMS) (R01GM085437); National Science Foundation (NSF) (ECS-9731293).

Acknowledgment. We thank Yoav Shechtman for helpful feedback on the manuscript, Andreas Gahlmann and Adam Backer for contributions at the beginning of this project, and James W. Conway for assistance with nanofabrication.

See [Supplement 1](#) for supporting content.

REFERENCES

1. L. S. Barak and W. W. Webb, "Diffusion of low density lipoprotein-receptor complex on human fibroblasts," *J. Cell Biol.* **95**, 846–852 (1982).
2. J. Gelles, B. J. Schnapp, and M. P. Sheetz, "Tracking kinesin-driven movements with nanometre-scale precision," *Nature* **331**, 450–453 (1988).
3. T. Schmidt, G. J. Schutz, W. Baumgartner, H. J. Gruber, and H. Schindler, "Imaging of single molecule diffusion," *Proc. Natl. Acad. Sci. USA* **93**, 2926–2929 (1996).
4. M. J. Saxton and K. Jacobson, "Single-particle tracking: applications to membrane dynamics," *Annu. Rev. Biophys. Biomol. Struct.* **26**, 373–399 (1997).
5. A. Kusumi, T. A. Tsunoyama, K. M. Hiroseawa, R. S. Kasai, and T. K. Fujiwara, "Tracking single molecules at work in living cells," *Nat. Chem. Biol.* **10**, 524–532 (2014).
6. E. Betzig, G. H. Patterson, R. Sougrat, O. W. Lindwasser, S. Olenych, J. S. Bonifacino, M. W. Davidson, J. Lippincott-Schwartz, and H. F. Hess, "Imaging intracellular fluorescent proteins at nanometer resolution," *Science* **313**, 1642–1645 (2006).
7. S. T. Hess, T. P. K. Girirajan, and M. D. Mason, "Ultra-high resolution imaging by fluorescence photoactivation localization microscopy," *Biophys. J.* **91**, 4258–4272 (2006).
8. M. J. Rust, M. Bates, and X. Zhuang, "Sub-diffraction-limit imaging by stochastic optical reconstruction microscopy (STORM)," *Nat. Methods* **3**, 793–796 (2006).
9. A. Sharonov and R. M. Hochstrasser, "Wide-field subdiffraction imaging by accumulated binding of diffusing probes," *Proc. Natl. Acad. Sci. USA* **103**, 18911–18916 (2006).
10. W. E. Moerner, "Microscopy beyond the diffraction limit using actively controlled single molecules," *J. Microsc.* **246**, 213–220 (2012).
11. M. F. Juette, T. J. Gould, M. D. Lessard, M. J. Mlodzianoski, B. S. Nagpure, B. T. Bennett, S. T. Hess, and J. Bewersdorf, "Three-dimensional sub-100 nm resolution fluorescence microscopy of thick samples," *Nat. Methods* **5**, 527–529 (2008).
12. G. Shtengel, J. A. Galbraith, C. G. Galbraith, J. Lippincott-Schwartz, J. M. Gillette, S. Manley, R. Sougrat, C. M. Waterman, P. Kanchanawong, M. W. Davidson, R. D. Fetter, and H. F. Hess, "Interferometric fluorescent super-resolution microscopy resolves 3D cellular ultrastructure," *Proc. Natl. Acad. Sci. USA* **106**, 3125–3130 (2009).
13. D. Aquino, A. Schönle, C. Geisler, C. V. Middendorff, C. A. Wurm, Y. Okamura, T. Lang, S. W. Hell, and A. Egner, "Two-color nanoscopy of three-dimensional volumes by 4Pi detection of stochastically switched fluorophores," *Nat. Methods* **8**, 353–359 (2011).
14. H. P. Kao and A. S. Verkman, "Tracking of single fluorescent particles in three dimensions: use of cylindrical optics to encode particle position," *Biophys. J.* **67**, 1291–1300 (1994).
15. B. Huang, W. Wang, M. Bates, and X. Zhuang, "Three-dimensional super-resolution imaging by stochastic optical reconstruction microscopy," *Science* **319**, 810–813 (2008).
16. S. R. P. Pavani, M. A. Thompson, J. S. Biteen, S. J. Lord, N. Liu, R. J. Twieg, R. Piestun, and W. E. Moerner, "Three-dimensional, single-molecule fluorescence imaging beyond the diffraction limit by using a double-helix point spread function," *Proc. Natl. Acad. Sci. USA* **106**, 2995–2999 (2009).
17. Y. Shechtman, S. J. Sahl, A. S. Backer, and W. E. Moerner, "Optimal point spread function design for 3D imaging," *Phys. Rev. Lett.* **113**, 133902 (2014).
18. A. Small and S. Stahlheber, "Fluorophore localization algorithms for super-resolution microscopy," *Nat. Methods* **11**, 267–279 (2014).
19. B. Rieger and S. Stallinga, "The lateral and axial localization uncertainty in super-resolution light microscopy," *ChemPhysChem* **15**, 664–670 (2014).
20. H. Deschout, F. C. Zanacchi, M. Mlodzianoski, A. Diaspro, J. Bewersdorf, S. T. Hess, and K. Braeckmans, "Precisely and accurately localizing single emitters in fluorescence microscopy," *Nat. Methods* **11**, 253–266 (2014).
21. R. E. Thompson, D. R. Larson, and W. W. Webb, "Precise nanometer localization analysis for individual fluorescent probes," *Biophys. J.* **82**, 2775–2783 (2002).
22. K. I. Mortensen, L. S. Churchman, J. A. Spudich, and H. Flyvbjerg, "Optimized localization analysis for single-molecule tracking and super-resolution microscopy," *Nat. Methods* **7**, 377–381 (2010).
23. A. Gahlmann, J. L. Ptacin, G. Grover, S. Quirin, A. R. S. von Diezmann, M. K. Lee, M. P. Backlund, L. Shapiro, R. Piestun, and W. E. Moerner, "Quantitative multicolor subdiffraction imaging of bacterial protein ultrastructures in 3D," *Nano Lett.* **13**, 987–993 (2013).
24. A. Yildiz and P. R. Selvin, "Fluorescence imaging with one nanometer accuracy: application to molecular motors," *Acc. Chem. Res.* **38**, 574–582 (2005).

25. A. Pertsinidis, Y. Zhang, and S. Chu, "Subnanometre single-molecule localization, registration and distance measurements," *Nature* **466**, 647–651 (2010).
26. J. C. Vaughan, S. Jia, and X. Zhuang, "Ultrabright photoactivatable fluorophores created by reductive caging," *Nat. Methods* **9**, 1181–1184 (2012).
27. J. Enderlein, E. Toprak, and P. R. Selvin, "Polarization effect on position accuracy of fluorophore localization," *Opt. Express* **14**, 8111–8120 (2006).
28. S. Stallinga and B. Rieger, "Accuracy of the Gaussian point spread function model in 2D localization microscopy," *Opt. Express* **18**, 24461–24476 (2010).
29. J. Engelhardt, J. Keller, P. Hoyer, M. Reuss, T. Staudt, and S. W. Hell, "Molecular orientation affects localization accuracy in superresolution far-field fluorescence microscopy," *Nano Lett.* **11**, 209–213 (2011).
30. M. P. Backlund, M. D. Lew, A. S. Backer, S. J. Sahl, and W. E. Moerner, "The role of molecular dipole orientation in single-molecule fluorescence microscopy and implications for super-resolution imaging," *Chem. Phys. Chem.* **15**, 587–599 (2014).
31. B. Hanser, M. Gustafsson, D. Agard, and J. W. Sedat, "Phase-retrieved pupil functions in wide-field fluorescence microscopy," *J. Microsc.* **216**, 32–48 (2004).
32. Y. Deng and J. W. Shaevitz, "Effect of aberration on height calibration in three-dimensional localization-based microscopy and particle tracking," *Appl. Opt.* **48**, 1886–1890 (2009).
33. R. McGorty, J. Schnitzbauer, W. Zhang, and B. Huang, "Correction of depth-dependent aberrations in 3D single-molecule localization and super-resolution microscopy," *Opt. Lett.* **39**, 275–278 (2014).
34. S. Jia, J. C. Vaughan, and X. Zhuang, "Isotropic three-dimensional super-resolution imaging with a self-bending point spread function," *Nat. Photonics* **8**, 302–306 (2014).
35. I. Koyama-Honda, K. Ritchie, T. Fujiwara, R. Iino, H. Murakoshi, R. S. Kasai, and A. Kusumi, "Fluorescence imaging for monitoring the colocalization of two single molecules in living cells," *Biophys. J.* **88**, 2126–2136 (2005).
36. A. Pertsinidis, K. Mukherjee, M. Sharma, Z. P. Pang, S. R. Park, Y. Zhang, A. T. Brunger, T. C. Südhof, and S. Chu, "Ultrahigh-resolution imaging reveals formation of neuronal SNARE/Munc18 complexes *in situ*," *Proc. Natl. Acad. Sci. USA* **110**, E2812–E2820 (2013).
37. M. A. DeWitt, A. Y. Chang, P. A. Combs, and A. Yildiz, "Cytoplasmic dynein moves through uncoordinated stepping of the AAA+ ring domains," *Science* **335**, 221–225 (2012).
38. J. R. James and R. D. Vale, "Biophysical mechanism of T-cell receptor triggering in a reconstituted system," *Nature* **487**, 227–230 (2012).
39. J. W. Goodman, *Introduction to Fourier Optics* (Roberts, 2005).
40. A. S. Backer and W. E. Moerner, "Extending single-molecule microscopy using optical Fourier processing," *J. Phys. Chem. B* **118**, 8313–8329 (2014).
41. J. Broeken, B. Rieger, and S. Stallinga, "Simultaneous measurement of position and color of single fluorescent emitters using diffractive optics," *Opt. Lett.* **39**, 3352–3355 (2014).
42. M. Born and E. Wolf, *Principles of Optics* (Cambridge University, 1999).
43. W. T. Welford, *Aberrations of Optical Systems* (Adam Hilger, 1986).
44. J. A. Kubby, *Adaptive Optics for Biological Imaging* (CRC Press, 2013).
45. K. F. Tehrani, J. Xu, Y. Zhang, P. Shen, and P. Kner, "Adaptive optics stochastic optical reconstruction microscopy (AO-STORM) using a genetic algorithm," *Opt. Express* **23**, 13677–13692 (2015).
46. D. Burke, B. Patton, F. Huang, J. Bewersdorf, and M. Booth, "Adaptive optics correction of specimen-induced aberrations in single-molecule switching microscopy," *Optica* **2**, 177 (2015).
47. G. Zheng, X. Ou, R. Horstmeyer, and C. Yang, "Characterization of spatially varying aberrations for wide field-of-view microscopy," *Opt. Express* **21**, 15131–15143 (2013).
48. M. P. Backlund, M. D. Lew, A. S. Backer, S. J. Sahl, G. Grover, A. Agrawal, R. Piestun, and W. E. Moerner, "Simultaneous, accurate measurement of the 3D position and orientation of single molecules," *Proc. Natl. Acad. Sci. USA* **109**, 19087–19092 (2012).
49. M. D. Lew, A. R. S. von Diezmann, and W. E. Moerner, "Easy-DHPSF open-source software for three-dimensional localization of single molecules with precision beyond the optical diffraction limit," *Protocol Exchange* (2013), doi: 10.1038/protex.2013.026.
50. L. S. Churchman and J. A. Spudich, "Colocalization of fluorescent probes: accurate and precise registration with nanometer resolution," *Cold Spring Harbor Protocols* **2**, 141–149 (2012).
51. D. Baddeley, D. Crossman, S. Rossberger, J. E. Cheyne, J. M. Montgomery, I. D. Jayasinghe, C. Cremer, M. B. Cannell, and C. Soeller, "4D super-resolution microscopy with conventional fluorophores and single wavelength excitation in optically thick cells and tissues," *PLoS ONE* **6**, e20645 (2011).
52. M. Erdelyi, E. Rees, D. Metcalf, G. S. K. Schierle, L. Dudas, J. Sinko, A. E. Knight, and C. F. Kaminski, "Correcting chromatic offset in multicolor super-resolution localization microscopy," *Opt. Express* **21**, 10978–10988 (2013).
53. S. Weisenburger, B. Jing, D. Hänni, L. Reymond, B. Schuler, A. Renn, and V. Sandoghdar, "Cryogenic colocalization microscopy for nanometer-distance measurements," *ChemPhysChem* **15**, 763–770 (2014).
54. F. Huang, T. M. P. Hartwich, F. E. Rivera-Molina, Y. Lin, W. C. Duim, J. J. Long, P. D. Uchil, J. R. Myers, M. A. Baird, W. Mothes, M. W. Davidson, D. Toomre, and J. Bewersdorf, "Video-rate nanoscopy using sCMOS camera-specific single-molecule localization algorithms," *Nat. Methods* **10**, 653–658 (2013).